UC Davis
UC Davis Electronic Theses and Dissertations

Title
Optical Devices in Medical Imaging and Industrial Automation

Permalink

Author
Srinath, Adithya

Publication Date
2022

Peer reviewed|Thesis/dissertation

Optical Devices in Medical Imaging and Industrial Automation

By

ADITHYA SRINATH
THESIS

Submitted in partial satisfaction of the requirements for the degree of

MASTER OF SCIENCE

in

Mechanical and Aerospace Engineering

in the

OFFICE OF GRADUATE STUDIES

of the

UNIVERSITY OF CALIFORNIA

DAVIS

Approved:

_____

Iman Soltani, Chair

_____

Barbara S. Linke

_____

Jonathon Schofield

Committee in Charge

2022

Abstract

This work deals with optical devices in medicine and industrial automation. The first chapter describes a design to integrate retinal imaging into a virtual reality headset. Conventional methods of retinal imaging require patients to sit still and follow instructions. The headset is meant to facilitate testing of toddlers and autistic children. The second chapter covers optics in industrial automation, specifically the localization of objects. The feasibility of a rapid, non-contact, high accuracy stereo vision system is explored. Active stereo vision using zoom and rotation of cameras is modelled. Inherent errors in sensors reduce the potential accuracy. This chapter calculates the highest possible accuracy achievable using off the shelf components, when the cameras are placed one - five meters away.

Contents

Organization

Chapter 1 is organized as follows. **Section 1.1** explains the motivation to integrate retinal imaging with a virtual reality headset. **Section 1.2** discusses existing methods, their limitations, challenges of retinal imaging and modelling the human eye. **Section 1.3** explains 2 ideas. The first design uses a phone screen for illumination where the polarity of light is manipulated to minimize losses. The second design uses a standalone source of illumination whose path can be controlled.

Chapter 2 is organized as follows. **Section 2.1** explains the target requirements and motivation. **Section 2.2** explains passive stereo vision. **Section 2.3** shows how passive stereovision can be improved. **Section 2.4** shows our calculation of the error in depth perception due to inherent errors in sensors. **Section 2.5** analyses the results of our calculations.

The appendix contains a detailed explanation of the anatomy of the human eye and the specifications of parts used to build and simulate the fundus imaging designs.

Chapter 1

Optics in Medicine

Fundus Imaging

1 Fundus Imaging

1.1 Introduction

Glaucoma is one of the leading causes of blindness worldwide [1]. It can be difficult for patients to recognize symptoms until late stages of the disease. Retinal imaging can be used to diagnose it [2]. A fundus camera is an optical device used to image the retina.

Retinal imaging can be done with the patients' pupil dilated or constricted depending on the camera used [3]. Mydriatic drops are used to dilate the pupil. The patient is instructed to look into the camera at a specified spot. Different fixation spots are used to image different sections of the retina. There is a flash of light and an image is taken. The flash can be uncomfortable, especially when the pupil is dilated. In addition, the mydriatic drops take a few hours to wear off.

It is challenging to get toddlers and autistic children to sit still for this test. With their pupils dilated, it is difficult to get them to fixate on a spot. The objective of this project is to explore integrating retinal imaging into a virtual reality headset to facilitate this process. This work focuses specifically on getting the illumination of the retina to work.

While a video is being played on the headset, images of the retina can be captured. By tracking the pupil, we can identify which section of the retina is being imaged. This report only discusses the optical challenges with designing the headset. Pupil tracking and image stitching is open to the future scope of the project.

1.2 Literature review

1.2.1 Methods of viewing the retina

Direct Ophthalmoscope

Until the 1850s it was generally accepted that the pupil is black because it completely absorbs light. Hemann Von Helmholtz realized that the retina reflects light [4]. He used this information to build the direct ophthalmoscope. It is a simple device that allows doctors to shine light through the pupil and view the retina. It does not require any refractive optical elements. The patients' cornea and crystalline lens act like a magnifying lens [4]. The doctor aligns their eye with the patients' eye and looks through the ophthalmoscope.

As seen in figure 1 modern ophthalmoscopes have rotary dials to control the size of the illumination [5]. Dilated eyes benefit from a wider beam of illumination. A vertical slit beam of light can also be used to identify the convexity of lesions on the retina. The direct ophthalmoscope provides a highly magnified view of the retina (14x magnification). High magnification has its purpose but makes it difficult for general examinations due to the limited field of view. Areas of the retina behind the iris cannot be viewed. The direct ophthalmoscope is difficult to use and needs fine motor skills and training

Figure 1: Direct Ophtalmoscope, image sourced from [5]

4

Indirect Ophthalmoscopes

Indirect ophthalmoscopes are also called binocular indirect ophthalmoscopes (BIO) [6]. A condensing lens is held by the ophthalmologist in front of the patients' eye. A real image of the retina is created between the patient and the ophthalmologist. The ophthalmologist views this image through a binocular headset. This allows depth perception which helps to diagnose retinal tears, holes and detachments. The illumination is provided by a lamp on the headset.
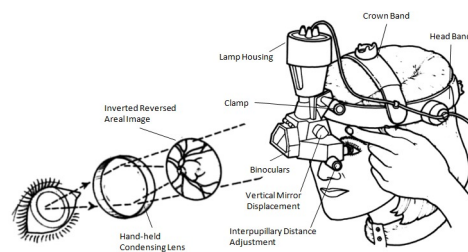

Figure 2: Binocular Indirect Ophthalmoscope, Image sourced from [6]

Fundus cameras

The fundus camera works on the same optical principles as the BIO [7]. An intermediate real image of the retina is created. A series of relay lenses and a camera take images of this image. There are variations in the illumination system. They can be broadly classified into external and internal illumination [7]. In an external illumination setup, the illumination path is uninterrupted. A beam splitter or ring mirror guides the light directly into the patients eye. The internal illumination system has the beam travel through the objective lens which causes back reflections from the lens surface.

Optical Coherence Tomography

Optical Coherence Tomography (OCT) works on the same principle as a michelson interferometer [8]. A coherent beam of light is split into two paths, a reference path and a sample path. The light in the reference path hits a reflector and returns. The light in the sample

path, hits the sample and returns. By analysing the interference in the reference ray and the sample ray, the distance to the sample path can be calculated.

This only works when the difference between the reference path and the sample path is less than one coherence length. The coherence length is the distance over which a wave maintains its coherence. For commercial OCT systems this is in the order of micrometers [9]. This process allows for depth estimation to map the topography of the retinal surface as well as deep tissue information. Unlike fundus imaging this is done point by point. Two rotating mirrors are required to scan the entire surface of the retina

1.2.2 Challenges illuminating the retina

There are many challenges with illuminating the retinal surface successfully [10].

1. The retinal surface has very low reflectivity. This varies between 0.1% to 10% depending on the wavelength of visible light used [10].

2. The corneal surface, ahead of the retina acts as a convex mirror. This creates a virtual image of a bright spot in front of the retina. This spot is commonly called the reflex of the eye. Clever techniques are used to avoid the reflex (see below).

3. The pupil contracts in the presence of bright lights which limits the light entering and leaving. Mydriatics can force the pupil to stay dilated. However, this is a source of discomfort to patients.

A common solution to avoiding the reflex is to use an annular source of light [10]. A ring shaped mirror to reflect the illumination keeps the central region of the eye free of light. This moves the corneal reflex outside the central region of the retina. There is the benefit of separating the illumination light path from the detection aperture. This reduces specular back reflections from optical surfaces in the eye and the fundus camera. A drawback of this method is the limitation in field of view. Only the central portion within the annular illumination can be imaged successfully. Multiple images with different orientations need to be taken to view larger sections of the retina.

1.2.3   Modelling the human eye
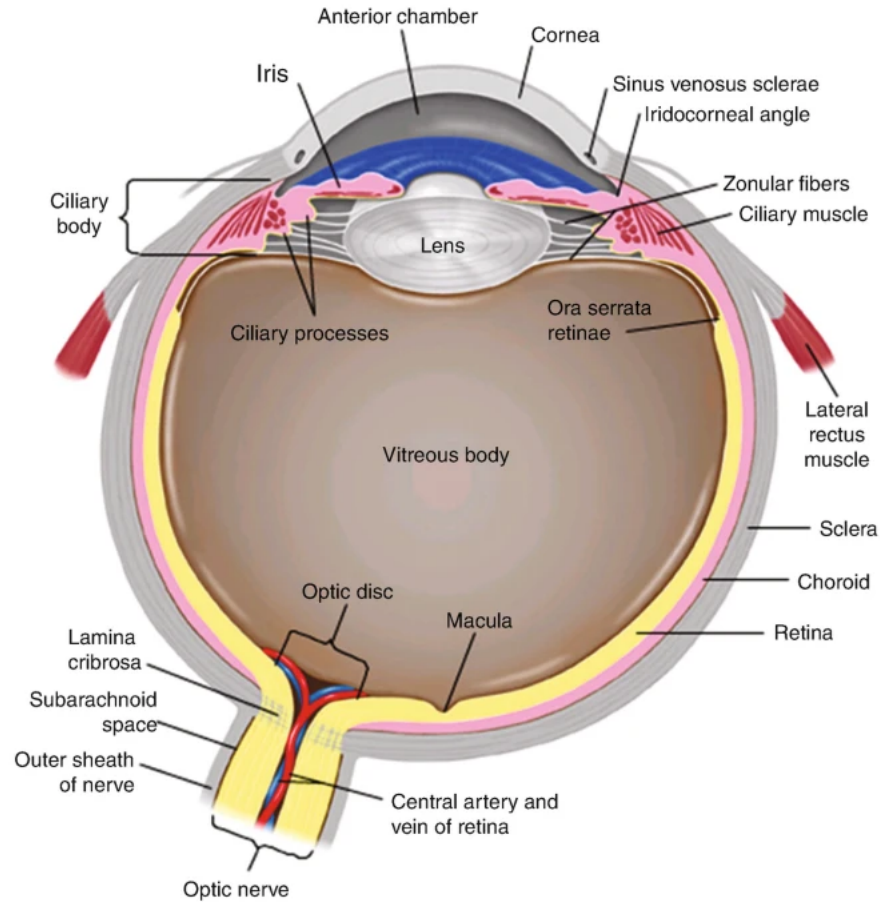

Horizontal section of the eyeball

Figure 3: Anatomy of the eye, image sourced from [11]

As shown in figure 3, the outermost portion of the eyeball is called the **cornea** [12]. It is clear and responsible for $\frac{2}{3}$ of the refractive power of the eye. Since it needs to be transparent, the cornea does not have blood vessels. It gets nourishment from the tear ducts and the aqueous humour. For detailed anatomy of the eye, please refer to section A

The **retina** is a circular disc located at the back of the eye. It has a diameter of 30 - 40 millimeters and a thickness of 0.5 millimeters. The **macula** is an oval shaped pigmented area on the retina, around 5 millimeters in width. It is responsible for central vision and has

a high density of photoreceptor cells. At the center of the macula, there is a small pit. This is called the **fovea** and is responsible for sharp central vision.

The **optic nerve** allows the eye to communicate with the brain. It is attached to the retina at the optic disc. Since this spot on the retina does not have photo receptor cells, human vision has a blind spot at the optic disc. The optic disc is highly prominent on a fundus image. It is used as a reference point while trying to orient fundus cameras [13].

The cornea and crystalline lens largely define the optical properties of the eye. Mathematical models of the eye leverage this [14]. The models vary based on the number of refractive surfaces that need to be modelled. More refractive surfaces improve the accuracy of the mode. However, it is recommended to use the simplest model that fits a project's requirements.

The **reduced eye** model only has a single refractive surface [15]. It is assumed that the crystalline lens, vitreous humour and aqueous humour do not contribute to the optical properties of the eye. To compensate for this, an extra powerful cornea with a power of 60 diopters, a radius of curvature of 5.55mm and a refractive index of $\frac{4}{3}$ is used. This makes it easier to model and closely resembles simple artificial eyes which can be used for testing. However, it is not a perfectly accurate model of the human eye and does not account for the relaxation/contraction of ciliary muscles. The ciliary muscles allow the eye to adjust its focal length.

The **simplified model** of the eye has three refractive surfaces. This is called the Elmsley-gullstrand model [14]. It uses one cornea and two lenses. The total power of the three surfaces add up to 60D. The surfaces are listed with the first being the outermost surface. The first surface is convex and has a radius of curvature of 7.8mm. It separates air from inside the eye. The refractive index across this surface changes from 1 to 1.336. The second

surface is convex and has a radius of curvature of 10 mm which can be adjusted upto 5.3mm to simulate the adjustment of eyes focal length. The refractive index across this surface changes from 1.336 to 1.413. The third surface is concave and has a radius of curvature of -6mm. The refractive index across this surface changes from 1.413 to 1.336.

The complexity increases in the **Le Grand's full theoretical eye** which has four refractive surfaces [16]. This is similar to the Elmsley-gullstrand model where the radius of curvature can be adjusted to simulate the accommodation of the eye. The refractive index of the eye is not constant throughout, there is a gradient with the center having a higher refractive index and the edges being lower. This gradient in the refractive index increases the effective power. The above models account for this by adjusting the refractive indices used to simulate the net effective power of a real eye. There is no intrinsic aperture stop to act as a pupil in any of these models.

1.3 Design, Experiment and simulations

The objective is to develop a fundus imaging device incorporated into a virtual reality headset. Ophthalmologists need an easier retinal imaging process for toddlers and autistic children. The current process requires the patient to follow instructions and may involve mydriatic drops. This section describes two design ideas to address this. Incorporating the retinal imaging setup into a virtual reality headset makes it easier for ophthalmologists. They do not need to give specific instructions, the headset can be worn and images are captured automatically, it does not depend on the patient to perform specific actions. Since these headsets require a screen, the first idea uses a phone screen for illumination. The second idea uses a stand alone illumination setup. The first design does not address the problem of using mydriatic drops. The second design allows control of the point of entry of the illumination rays at the pupil (as described later). If the point of entry at the pupil is within the size of a constricted pupil, mydriatic drops are not required.

1.3.1 Using a phone screen for illumination

To integrate a VR headset with fundus imaging, a beam splitter is essential. Beam splitters allow a portion of light to pass through and reflect the rest (section B.6). As shown in figure 4, some of the light from the phone passes through the beam splitter and enters the eye. The reflected rays hit the beam splitter. A portion of the reflected rays are channeled toward the camera at the beam splitter.

A large portion of light is lost using regular beam splitters. Polarized beam splitters are more efficient, they allow p-polarized light through and reflect s-polarized light. By rotating the polarizing beam splitter we can change which polarization is reflected and transmitted.

Liquid crystal displays (LCD) emit circularly polarized light [17]. By modifying the polarity of light and using a polarizing beam splitter these losses can be significantly reduced. Since
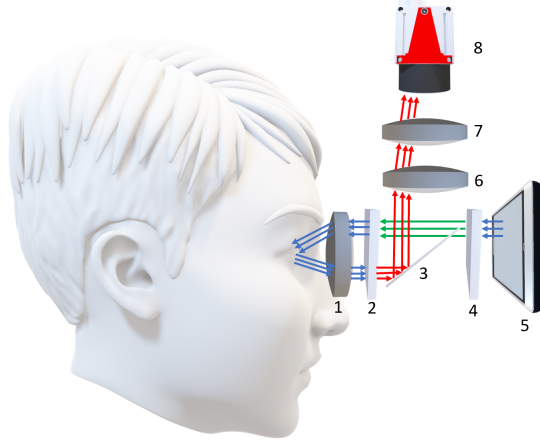
Figure 4: Design using light from phone as a source of illumination. Parts 1 - 8 are objective lens, $\frac{\lambda}{4}$ waveplate, polarizing beam splitter, $\frac{\lambda}{4}$ waveplate, phone, relay lens 1, relay lens 2, camera. The blue rays represent circularly polarized light, green is p-polarized, red is s-polarized.

the polarity of light is carefully controlled, a polarizer can remove stray light.

Following the rays from figure 4, circularly polarized light is emitted from the phone screen. It passes through a $\frac{\lambda}{4}$ waveplate (section B.5) which converts the light to p-polarized. The beam splitter is oriented to let p-polarized light pass through. The light then travels through another $\frac{\lambda}{4}$ waveplate which converts the light to circularly polarized. The circularly polarized light travels through the VR headset lens and illuminates the retina. The reflected rays would travel back through the VR headset lens and the $\frac{\lambda}{4}$ waveplate. The reflected rays are converted to s-polarized and reflect off of the beam splitter. This setup allows us to provide separate channels for illumination and imaging by controlling the polarity of light. The reflected rays pass through a series of lenses and enters the camera. These lenses are used to focus the light and allow a more compact setup.

The setup as shown in figure 4 was built on an optical breadboard as seen in figure 5. The virtual reality lens has a diameter and focal length of 50 millimeters (section B.1). The beam-splitter used is a polarizing beam splitter sold by Edmund Optics (Part number: 48-

545, New Jersey, USA). It is a square plate with a side of 2.5 centimetres and a thickness of 0.7 millimeters. A larger polarizing beam splitter would provide a higher field of view, however this is the largest one available off the shelf. Off the shelf lens mounts are typically adjustable and large, 3D printed mounts were designed to keep the system compact.

To test our setup, we used an artificial eye (section B.4). It is commonly used to train ophthalmologists on the ophthalmoscopes. It resembles the simplified eye model using only a single lens to simulate the cornea. At the back of the model, there is a plate with an image of the retinal surface. This image can also be replaced with a grid to help with measuring the field of view.
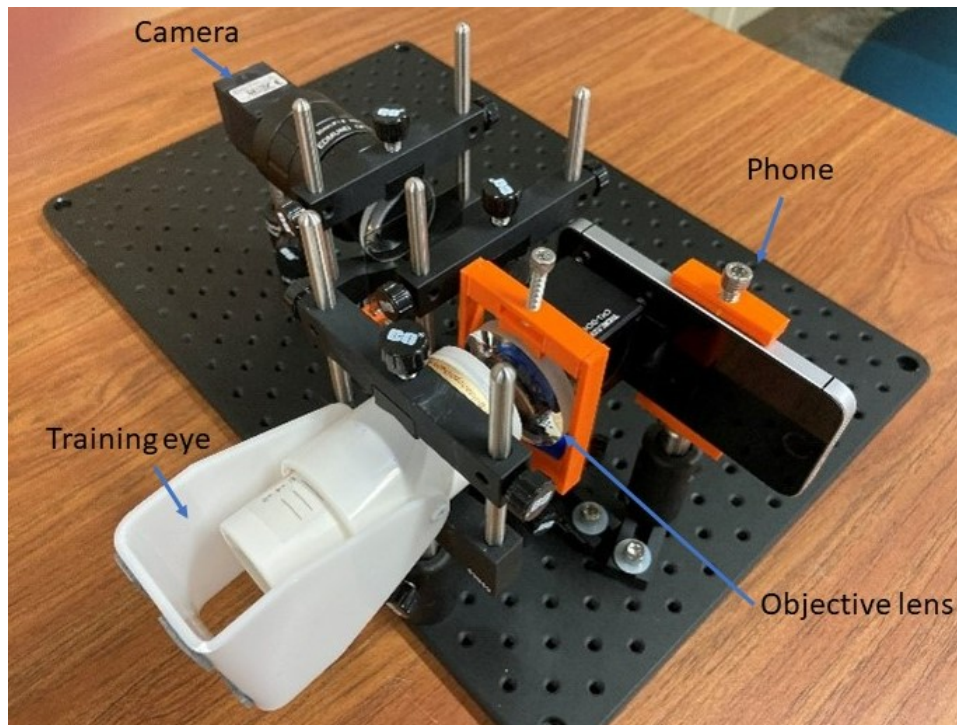

Figure 5: Experimental setup on an optical breadboard

Results

This was a feasibility test. A good image should show the optic disc and vasculature clearly.

Our experiments with the artificial eye showed promising results (figure 6). The retina of the artificial eye was visible using just the phone screen for illumination. The optic disc and veins were clearly visible. However we could not view the optic disc clearly while testing with our own eyes. Two pairs of healthy human eyes were unable to provide a clear image of the optic disc. Even with the assistance of mydriatic eye drops to dilate our pupils and additional lighting we did not get quality images with this setup.
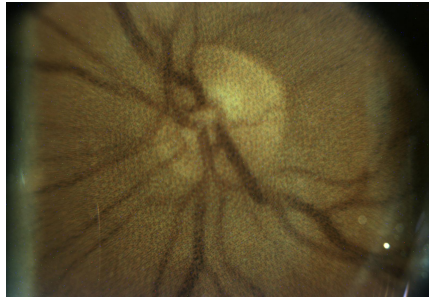

Figure 6: Image obtained from setup described in figure 5

Conclusions

This design is not feasible because phone screens do not provide enough illumination. Our initial design did not account for the following.

1) **The extremely poor reflectivity of the retinal surface**; The plate on the artificial eye is highly reflective compared to a human retina. We were able to distinguish the optic disc and veins using only a phone screen as illumination.

2) **The illumination axes needs to be close to the optical axis**; There is very little margin for error in the displacement between the optical axes of the illumination beam and the pupil. Illumination beams that enter the far retina away from the optical axis will not reflect out from the eye.

3) **The effect of the cornea on the illumination beam**; As the illumination light rays pass through the cornea, they converge. Testing with a flashlight instead of a phone, we could only illuminate a small portion of the human retina.

1.3.2   Using a dedicated source of illumination

We improved upon our initial design by adding a separate illumination source, a larger beam splitter and scanning the retina in sections instead of one large image. This design is based on [18]. Using an external illumination source allows us to proceed without modifiying the polarity of light. A strong source of light can be used to accomodate losses. This setup is insensitive to polarization of light. As an optional improvement, polarization of light can be used in the future to minimize the effect of back reflections and stray light. Back reflections are specular in nature. The polarization is maintained. If the polarization of illumination is controlled, the back reflections will have the same polarization and can be filtered

As shown in figures 7a and 7b, a rotating mirror can adjust which section of the retina is illuminated. When this mirror makes an angle of 45 degrees with the vertical, the central section of the retina is illuminated. Because the mirror is offset by 1.5mm from the optical axis, the illuminated region is also slightly offset. Simulations using a python library called pyoptools [19] showed that, at 36 degrees, the top section of the field of view is illuminated. At 53 degrees the bottom of the field of view is illuminated.

The optics have been adapted to mimic a 4f optical relay system as shown in figure 8. Four components are placed one focal length away from each other, giving it the name '4f'. This design uses two lenses with the same focal length. The eye is placed one focal length away from the virtual reality headset lens. A relay lens is placed two focal lengths away from the virtual reality headset lens. The illumination beam is projected from one focal length away. The total length of the system is four focal lengths.

The 4f optical relay system preserves the etendue (spread) of the illumination beam. By using the same focal length lenses, the system also maintains a 1:1 magnification. This makes it easy to control the position of the illumination at the pupil. Since the etendue is
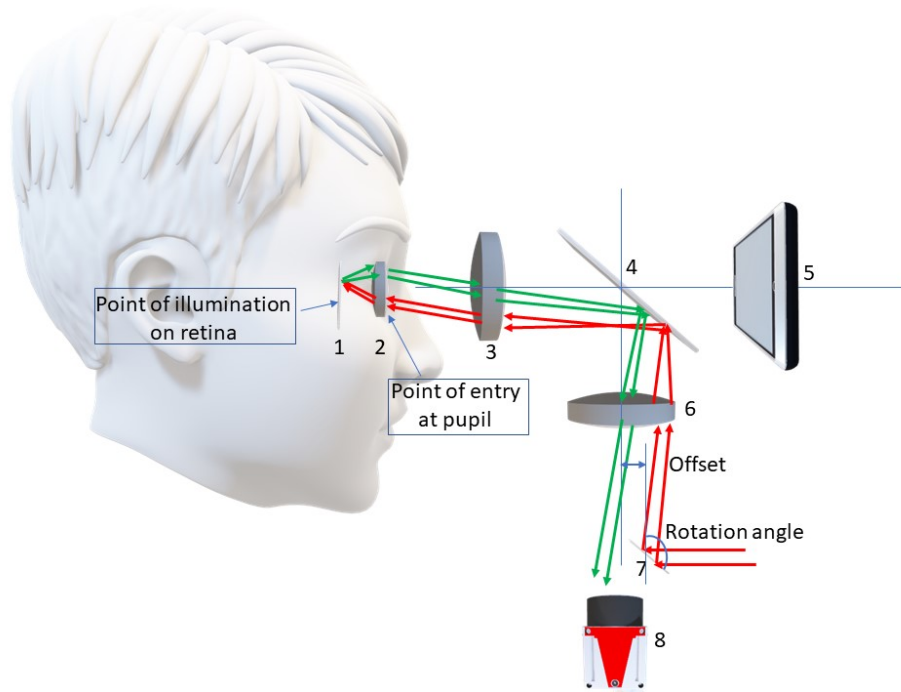
(a) Rotating mirror set to illuminate top section of retina
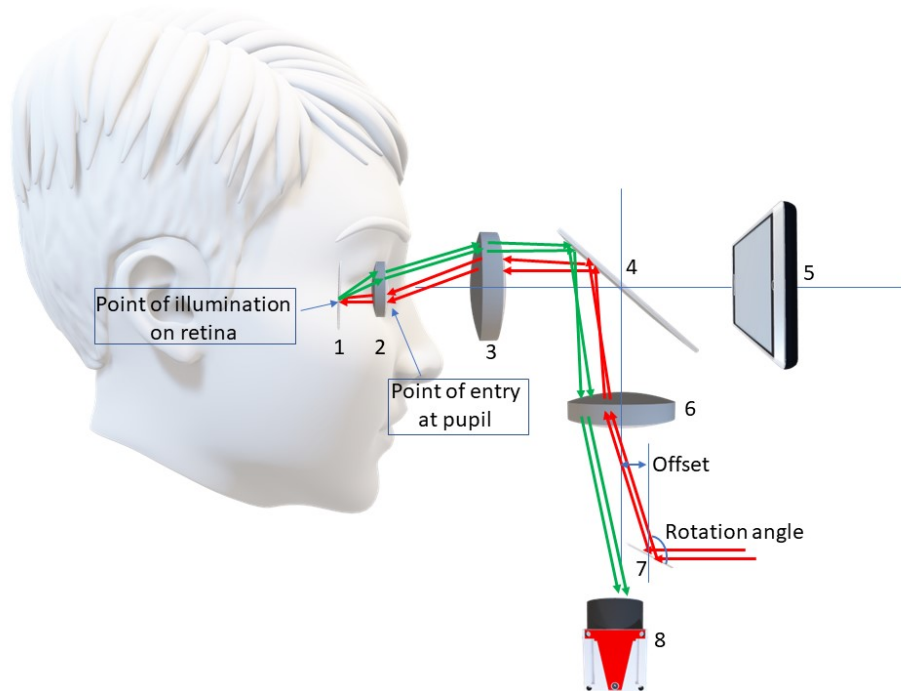
(b) Rotating mirror set to illuminate bottom section of retina

Figure 7: The red rays indicate path taken by illumination source. The green rays indicate path taken after reflection from the retina. Parts 1-8 are retina,cornea,objective lens, beam splitter, phone, relay lens, rotating mirror, camera respectively
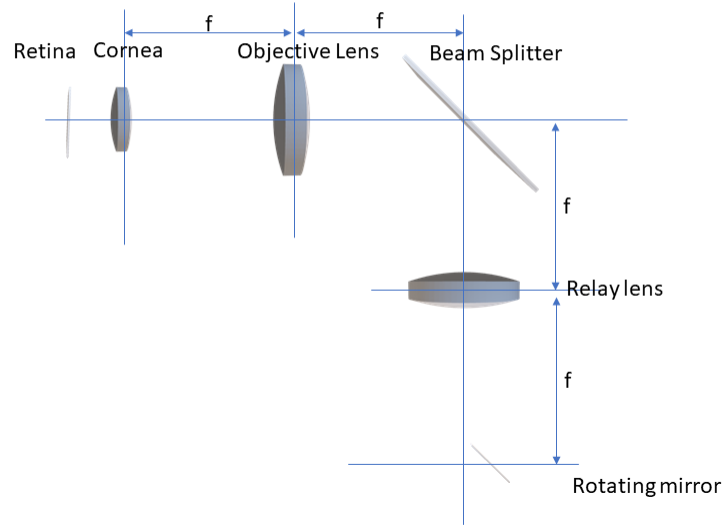
Figure 8: 4f optical relay system

preserved through the relay system, it is possible to easily control the etendue close to the eye by adjusting the etendue of the source.

The retina is divided into segments for imaging, rather than taking a single large image. The smaller segments can be stitched together. A rotating mirror illuminates the retina segment by segment. By changing the angle at which the illumination enters the pupil, different segments are illuminated. This provides two advantages. First, it allows us to work around the limitation of using an annular source (as described in section 1.2.2). The size of the annular beam is limited by the size of the pupil. This limits the field of view, especially with non dilated pupils. Second, the future scope of this project includes incorporating an OCT scanner which scans the retina point by point. The rotating mirror used in this design will streamline the integration process. By illuminating the retina in sections we might be able to avoid distracting patients while they are watching the virtual reality media content.
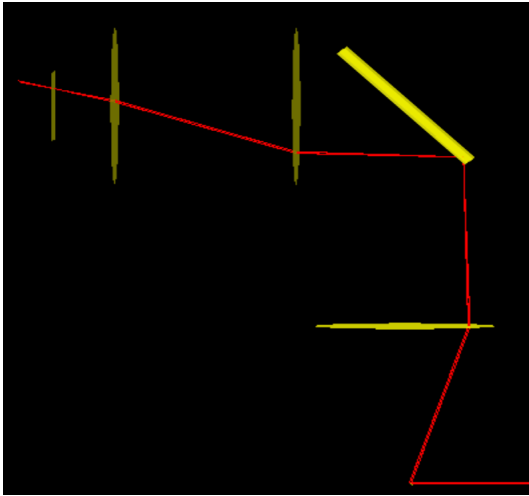
18

Results

A physical test setup of this design was not built, it was only simulated. Simulations of the design were run using pyoptools [19], an optics modelling library for python. A 50mm focal length lens with a diameter of 50mm is used as both the objective and relay lens. A 2mm x 2mm rotating mirror and a 50mm x 50mm beam splitter was modelled. The beam splitter was selected as it is the largest that can be fit into the headset. This is explained in section B.6. The dimensions of the rotating miror are constrained by the offset of the mirror from the optical axis.Ray tracing is used to pass light through all the optical components. Using the information in figure 8 and section B these results can be replicated. The diameter of the pupil was taken to be 4mm. A constricted pupil has a diameter of 2 - 4 mm and a dilated pupil has a diameter of 4 - 8 mm.
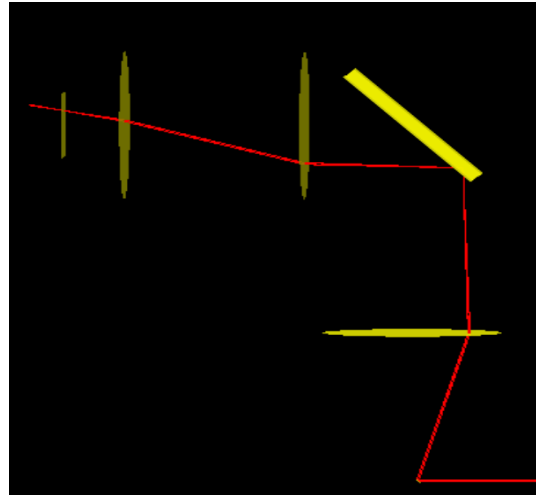
As shown in figure 9, different angles of rotation of the small mirror illuminate different sections of the retina. After running simulations for the range 36 - 54 degrees, the results in table 1 were obtained. It lists the position on the retina and pupil for different angles of rotation. A negative position on the retina indicates that the point falls below the optical axis.

| Simulation results		
Rotation angle with vertical (degrees)	Illumination position on retina measured from the optical axis(mm)	Point of entry of illumination on the pupil measured from the optical axis(mm)
36	5.52	1.50
37	4.87	1.50
38	4.24	1.50
39	3.61	1.50
40	2.99	1.50
41	2.39	1.50
42	1.78	1.50
43	1.18	1.50
44	0.59	1.50
45	0	1.50
46	-0.59	1.50
47	-1.18	1.50
48	-1.78	1.50
49	-2.39	1.50
50	-2.99	1.50
51	-3.61	1.50
52	-4.23	1.50
53	-4.87	1.50
54	-5.52	1.50

Table 1: Simulation results

(a) 36 degrees

(b) 37 degrees
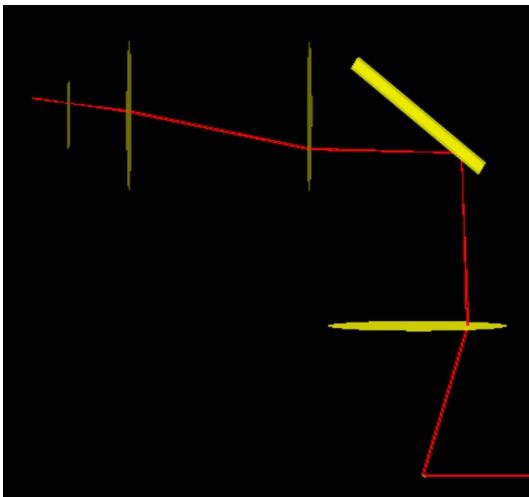
(c) 38 degrees
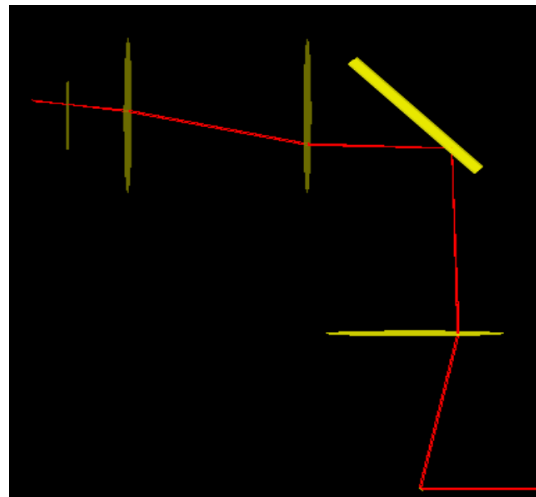
(d) 39 degrees

Figure 9: Simulated results using pyoptools

(a) 40 degrees

(b) 41 degrees
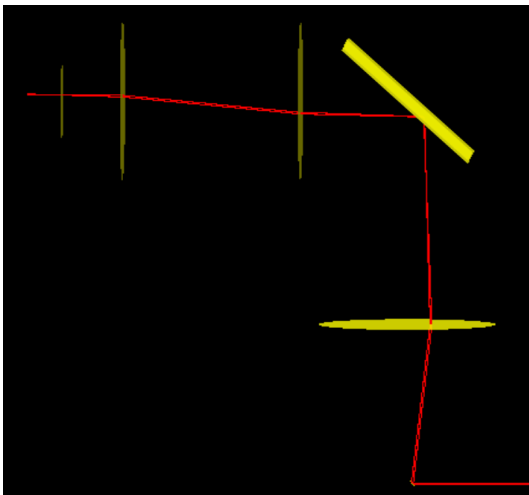
(c) 42 degrees

(d) 43 degrees
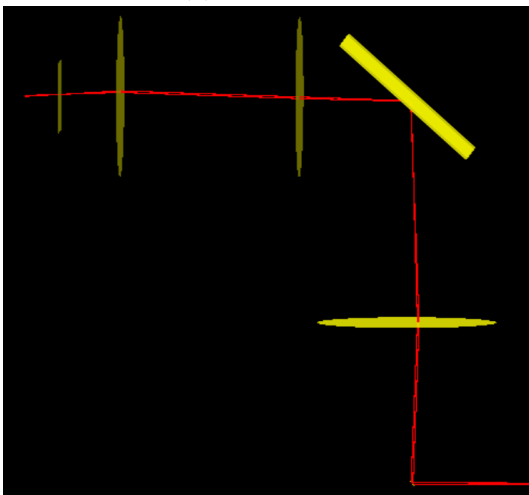
(e) 44 degrees
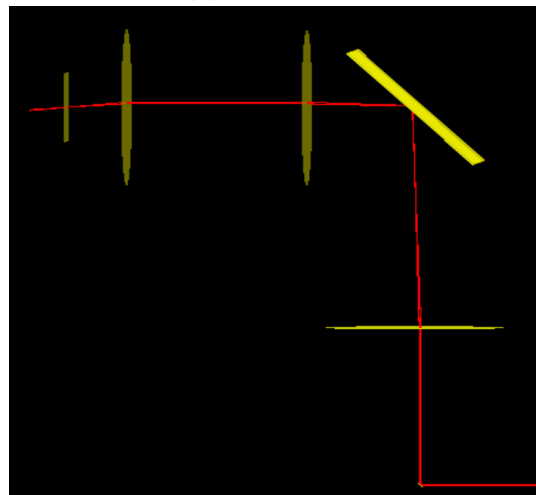
(f) 45 degrees

Figure 10: Simulated results using pyoptools
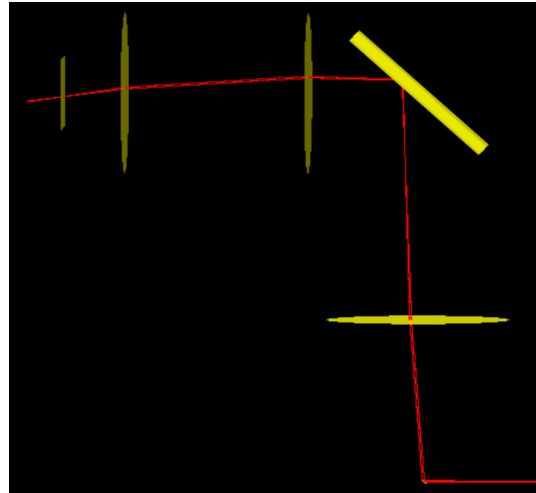
(a) 46 degrees   (b) 47 degrees
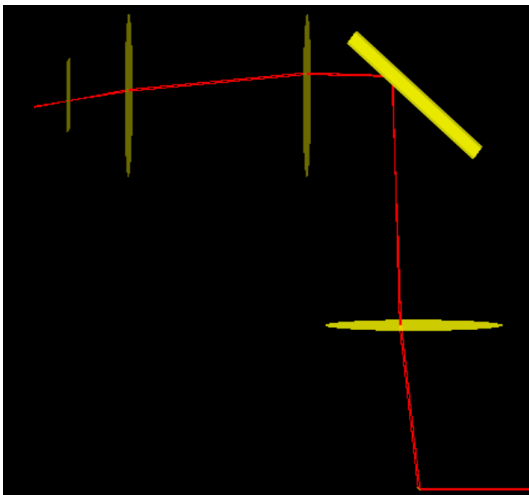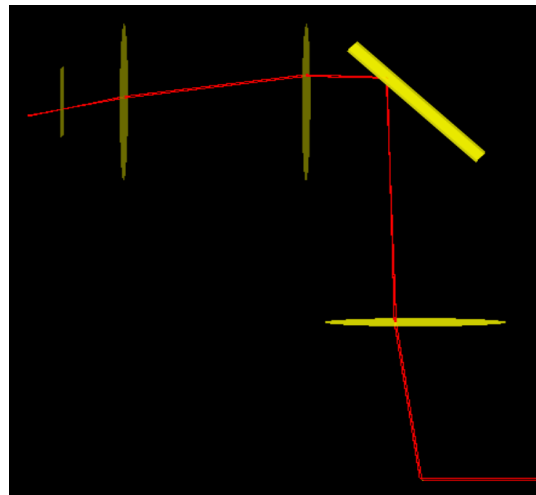
(c) 48 degrees   (d) 49 degrees
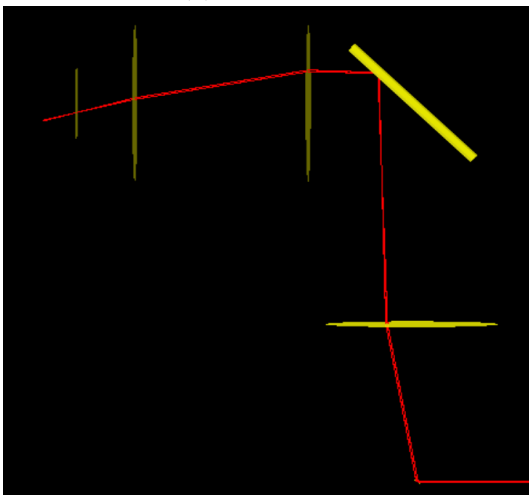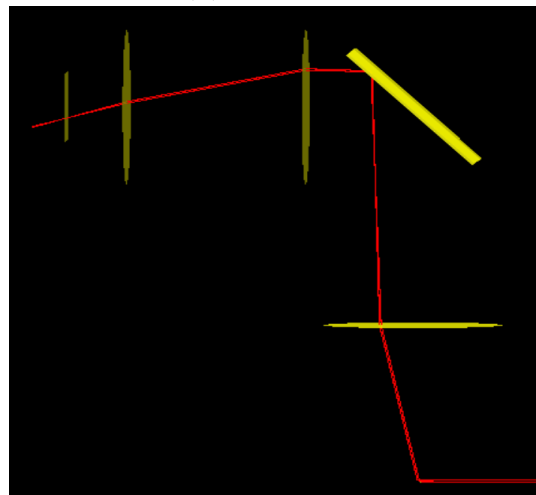
(e) 50 degrees   (f) 51 degrees

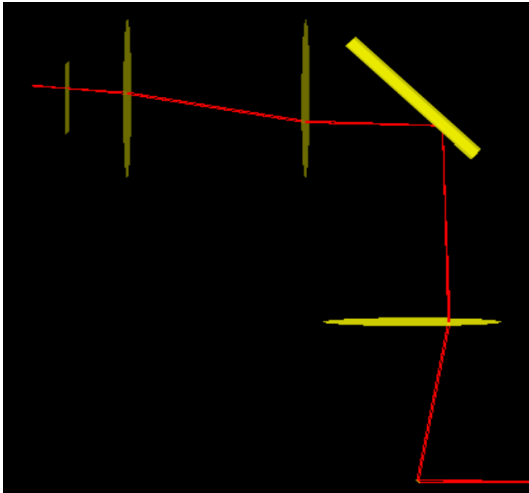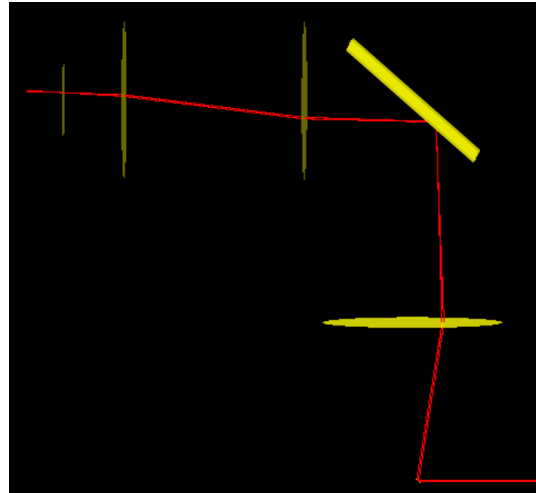Figure 11: Simulated results using pyoptools

(a) 52 degrees

(b) 53 degrees

(c) 54 degrees

Figure 12: Simulated results using pyoptools
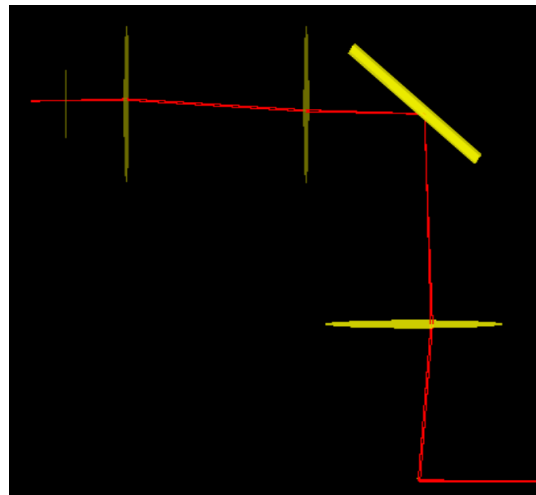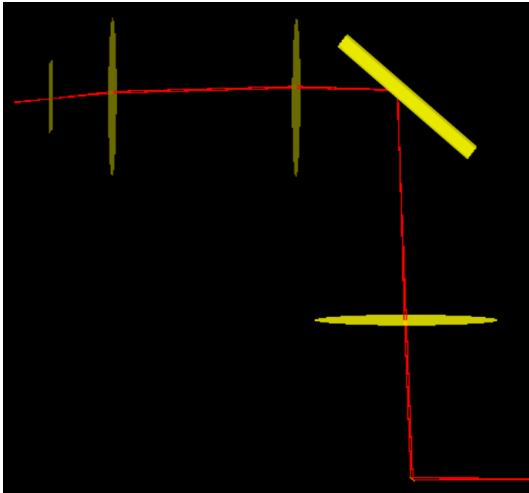
Position on retina against rotation angle
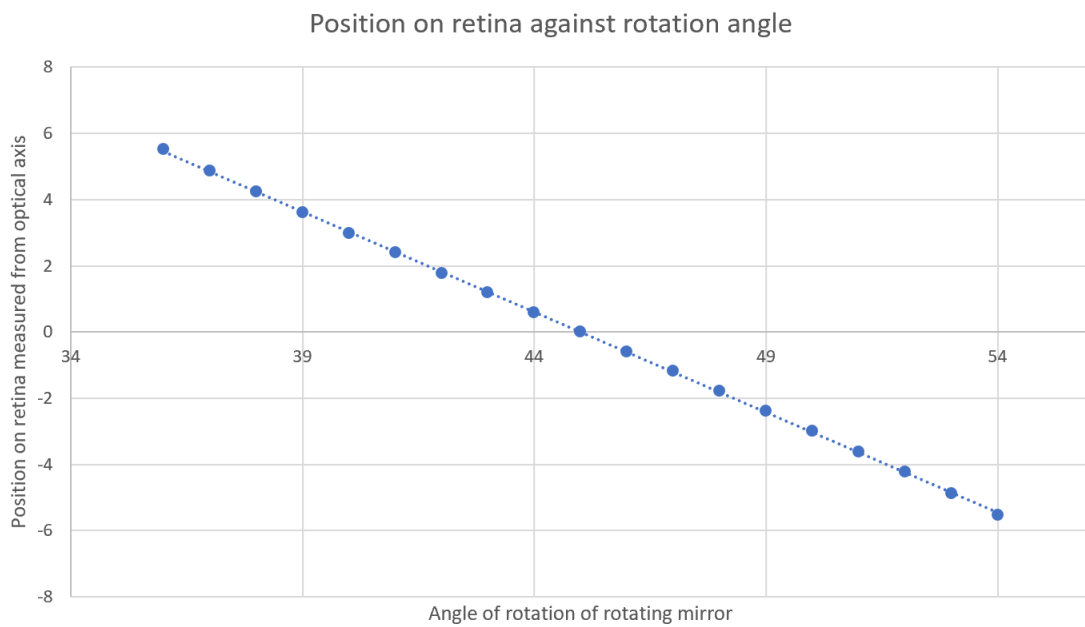
Figure 13: Graph showing consistent movement of retinal illumination position with rotation of the mirror (represented as part 7 in figure 7). Y axis shows the position on the retina in mm, x axis shows the angle of rotation of the mirror in degrees.

Conclusions

Figure 13 shows that there is a linear relation between the rotation of the mirror and position on retina. This is desirable, it shows that a constant rate of rotation will result in a constant scanning rate at the retina.

Table 1 shows that the point of entry at the pupil is constantly at 1.5mm. This relates to the offset of the rotating mirror from the optical axis, also at 1.5mm. A constricted pupil has a diameter of 2-4mm and a dilated pupil has a diameter of 4-8mm. By reducing the offset further, it is possible to use this design to image constricted pupils without mydriatic drops. The design will need to be adjusted to accomodate a smaller scanning mirror. Alternatively, by using a different relay lens the magnification of the relay system can be changed.

These results show how a stripe of light can be scanned over the retina to illuminate it section by section. It shows good potential for use in non dilated eyes and controlling the position of the light.

1.4 Future scope

It is possible to integrate a fundus imaging apparatus with a virtual reality headset using the design in section 1.3.2. This work discussed optical design ideas to control the illumination of the retina.

This design requires images to be taken section by section. In the future these images will need to be stitched together. The scanning should be controlled such that there is an overlap between sections to allow for stitching. Alternatively a rolling shutter camera can be synced with the scanning mirror. They need to be synced such that the rotation of the mirror happens between lines of pixels being triggered.

The idea of manipulating polarity of light to reduce losses, also helps reduce back reflections and unwanted scatter. As mentioned earlier, back reflections are specular in nature. The polarization is maintained. If the polarization of illumination is controlled, the back reflections will have the same polarization and can be filtered. If required these can be integrated with the design from section 1.3.2.

Pupil tracking needs to be integrated for multiple reasons. If the eye moves when images are being taken, those set of images can no longer be used. Additionally, the pupil needs to be tracked to identify which section of the retina is being imaged. A small shift in the pupil will result in a different section of the retina being imaged.

Once reliable fundus images can be taken, an OCT setup can be integrated with this. The existing rotating mirror will still be used to scan in the y-axis. An additional rotating mirror for the OCT laser to scan in the x-axis will also need to incorporated.

Simultaneous fundus and OCT imaging will allow ophthalmologists to correspond 2D color

fundus images with the volume images (depth and topography) in the same region.

Chapter 2

Optics in Industrial Automation, Stereo Vision

2 Stereo vision

2.1 Introduction

The objective of this section is to explore the feasibility of a rapid, non-contact method to localize and measure objects precisely using cameras. Quality control is a repetitive task which requires high attention to detail. Human beings get fatigued doing this over a long period of time and make mistakes [20]. Automating quality control will increase reliability. There are many methods of doing this, stereo vision was chosen because cameras allow identification and tracking of objects which make it good for automation. The requirements to meet are as follows. The objects can be stationary or mobile. The initial target measurement error was set to 100 microns while measuring an object five metres away. The measurement error was selected so that the setup can be used for quality control of manufactured parts with a tolerance in the hundreds of microns. The distance was selected to to give the setup an option of being mounted above the samples. This section discusses the challenges meeting this target and what is possible with existing off the shelf technology.

Stereopsis is the ability to augment two-D vision with depth perception [21]. When two images are taken of an object from different angles, it is possible to estimate the distance to the object. There is a disparity in the position of the object in the two images. Images closer to the cameras will have a higher disparity. Measuring the disparity provides depth estimates.

The human eye uses the same principle to estimate depth. While holding a pen close to the eye, view it with the left eye closed and then view it with the right eye closed. The pen appears to jump between images but objects far away do not move as much.

Using a zoom and rotation system to augment the performance of stereo vision is considered in this work. As explained in section 2.3 using a zoom system requires camera rotation. Cam-

eras are used as opposed to other methods such as interferometry to allow easier automation and tracking of objects.

2.2 Passive stereovision
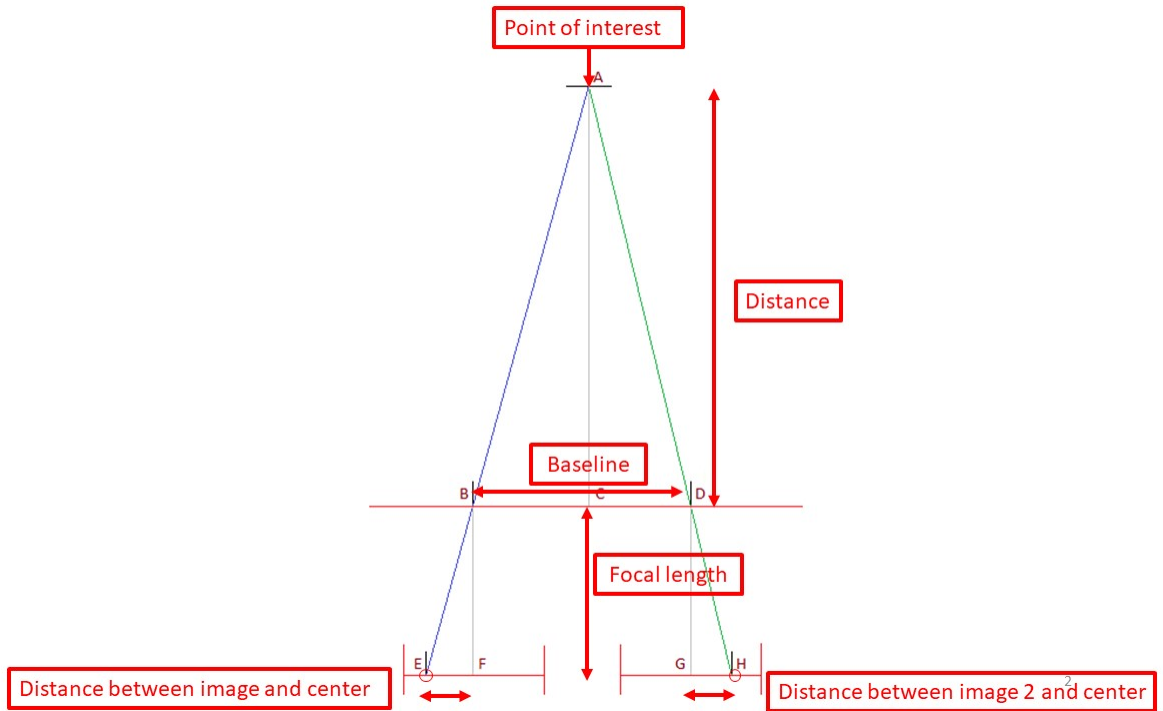
Figure 14: Using passive stereovision for depth estimation. B and D represent the camera centers, F and G represent the center of the image sensors. E and H show the location of the image on the sensor. The disparity is the difference between EF and GH

From figure 14 we see that the baseline and focal length are predetermined factors that can be controlled. The distance can be calculated using equation 1 [22].

$$Distance = \frac{Baseline * Focallength}{Disparity} \tag{1}$$

Depth estimation using steropsis loses accuracy as the depth increases. If the disparity between images is less than one pixel, it cannot be detected. The higher the disparity relative to pixesl, the higher the accuracy of depth estimation. To overcome this, active stereovision can be used, discussed in the following section.

2.3　Active Stereovision

Active stereovision in this work focuses on zoom and rotation [23]. Structured light is another example of active stereovision [24] but outside the scope of this work. The accuracy of stereovision is propotional to the number of pixels an object occupies. To get an object to occupy more pixels, the cameras need to zoom in. Increasing the focal length of the cameras is the equivalent of zooming in. Variable focal length lenses can be used to achieve this.

As shown in figure 15, when the focal length increases, the field of view of each of the two cameras reduces. The overlap between their respective fields of view also reduces. When the cameras zoom in too far there may be no more overlap. Both cameras need to be viewing the object to use steropsis. To maintain an overlap in the fields of view as the cameras zoom in, rotation of cameras is required.
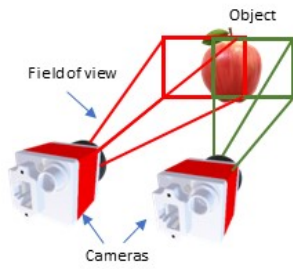
(a) Passive Stereovision
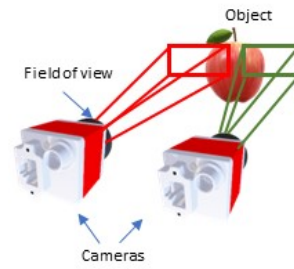
(b) Zoomed in to improve accuracy
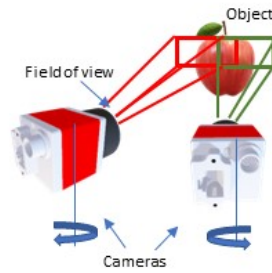
(c) Rotating the zoomed in fields of view for overlap

Figure 15: Necessity of rotation while changing focal length

2.4 Estimating uncertainty in depth perception

Actuators are required to rotate the cameras. Sensors are needed to keep track of how much the camera has rotated. There exist inherent uncertainties in sensors and actuators. They compound and result in some error in depth perception. This section explores the feasibility of meeting a target error of 100 microns at a distance of five metres. The calculations in this section are based on off the shelf components.This calculation is performed in two dimensions, assuming that the camera platform is fixed and incapable of pitching up and down. Only tracking an object in the x-y plane is considered. The camera and object are on the same z co-ordinate. Table 2 defines all the parameters used in this calculation.

The sources of error are as follows.

1. The first source of error is rotation accuracy. The cameras are rotated by a rotary actuator and a built in rotary encoder reads the rotation. The PRS 200 rotary actuator with encoder made by Physik Instrumente was considered.

2. The second source of error is the focal length adjustment accuracy. The zoom lenses are a simple two lens setup [25] with a linear actuator separating them. The accuracy of adjusting the focal length is dependent on the accuracy of the linear actuator. The L-406 linear actuator with encoder made by Physik Instrumente was considered.

3. The third source of error is the size of a pixel. When an object occupies a pixel, the exact location within the pixel cannot be identified. This will result in a maximum error of half a pixel length on the image sensor. The Basler a2A3840 camera with a pixel size of 2 microns was considered for this.
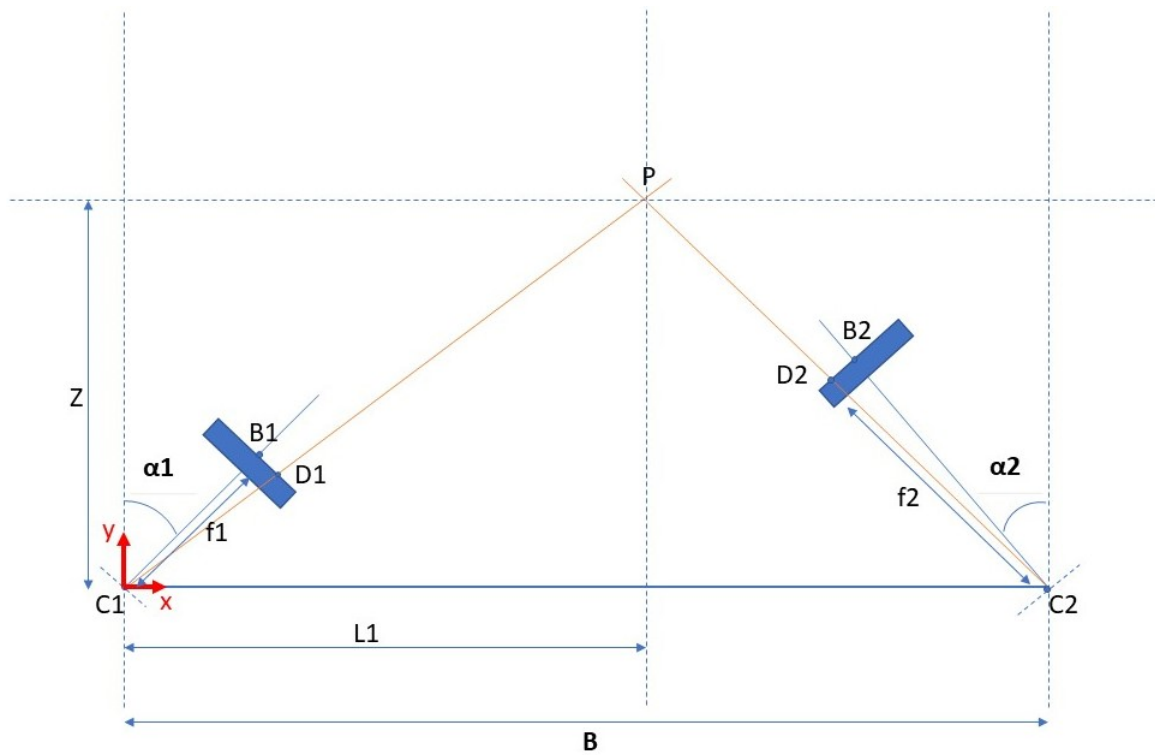
Figure 16: Top view of the setup. C1 and C2 represent the cameras optical centers. P represents the point of interest whose depth (distance to object) we are trying to ascertain. Other parameters have been defined in Table 2
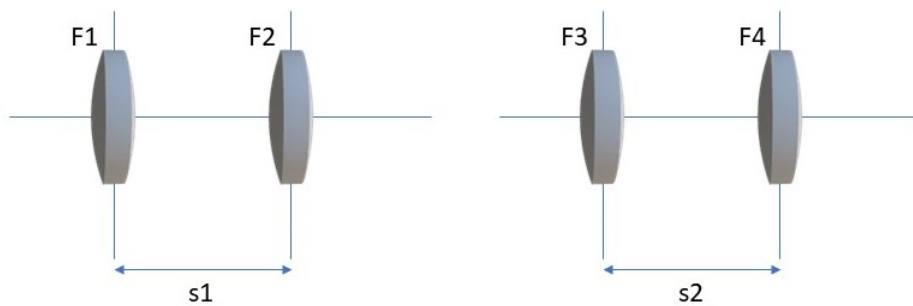
Figure 17: From left to right, the figures represent the simple zoom systems for cameras 1 and 2 respectively. 'F' is the focal length of the lens. 's' is the separation distance.

Defining symbols	
Symbol	Parameter
C1	Center of rotation of left camera
C2	Center of rotation of left camera
α_1	Angle of rotation of left camera
α_2	Angle of rotation of right camera
B	Baseline, distance between the cameras
P	Point of interest
L1	Horizontal distance between C1 and P
Z	Depth, vertical distance between C1 and P
d_1	Distance between B1 and D1
d_2	Distance between B2 and D2

Table 2: Defining symbols used in derivation

To switch to a coordinate system, 'C1' will be used as the origin. Moving from C1 to C2 increases the x axis. Both cameras are looking at the same point 'P'. Point 'P' need not be in the center of the frame of either camera (refer figure 16). Points 'D1' and 'D2' represent the position of the image of 'P' on the camera sensor. The distance between the centers (C1,C2) and their respective sensors (B1,B2) represent the respective focal lengths.

Using trigonometry, we calculate the co-ordinates of D1 to be

$$D1_x = f_1 * sin(\alpha_1) + d_1 * cos(\alpha_1)$$

$$D1_y = f_1 * cos(\alpha_1) - d_1 * sin(\alpha_1)$$

Similarly we can figure out the coordinates for D2

$$D2_x = b - f_2 * sin(\alpha_2) - d_2 * cos(_2)$$

$$D2_y = f_2 * cos(\alpha_2) - d_2 * sin(\alpha_2)$$

Next we plot a line from C1 to D1 and another line from C2 to D2. The point of intersection of these lines tell us the co-ordinates of 'P'

37

Line equation C1-D1

$$y = \frac{(f_1 * cos(\alpha_1)) - (d_1 * sin(\alpha_1))}{(f_1 * sin(\alpha_1)) + (d_1 * cos(\alpha_1))} * x \tag{2}$$

Line equation for C2-D2

$$y = \frac{(f_2 * cos(\alpha_2)) - (d_2 * sin(\alpha_2))}{(-f_2 * sin(\alpha_2)) - (d_2 * cos(\alpha_2))} * (x - b) \tag{3}$$

The point of intersection of these two lines (equations 2, 3) is represented by equations 6, 7. The equation had to be split owing to the size.

$$x1 = b * ((d_2 * sin(\alpha_2) - f_2 * cos(\alpha_2)) * (f_1 * sin(\alpha_1) + d_1 * cos(\alpha_1)) \tag{4}$$

$$x2 = ((f_1 * cos(\alpha_1) - d_1 * sin(\alpha_1)) * (-f_2 * sin(\alpha_2) - d_2 * cos(\alpha_2))$$
$$- (f_2 * cos(\alpha_2) - d_2 * sin(\alpha_2)) * (f_1 * sin(\alpha_1) + d_1 * cos(\alpha_1)) \tag{5}$$

$$L1 = \frac{x1}{x2} \tag{6}$$

$$z = \frac{f_1 * cos(\alpha_1) - d_1 * sin(\alpha_1)}{f_1 * sin(\alpha_1) + d_1 * cos(\alpha_1)} * L1 \tag{7}$$

Equation 7 gives the depth of point 'P' as a function of rotation, focal length and pixel size. Next, from figure 17, the focal length is related to the separation distance between the two lenses to account for linear positioning uncertainty.

Using the compound lens equation:

$$f1 = \frac{F1 * F2}{F2 + F1 - s1} \tag{8}$$

$$f2 = \frac{F3 * F4}{F3 + F4 - s2} \tag{9}$$

Plugging in equations 8 and 9 into 7 expresses depth of point 'P' as a function of rotation, linear position and pixel size. Partial derivatives are used to calculate the individual effect of each parameters uncertainty, on depth perception. Δ is used to represent error. δ is used as the partial derivative operator. z is the y axis distance to the object.

$$\Delta z = \frac{\delta z}{\delta \alpha_1} * \Delta \alpha_1 \qquad\qquad \Delta z = \frac{\delta z}{\delta \alpha_2} * \Delta \alpha_2 \tag{10}$$

$$\Delta z = \frac{\delta z}{\delta s_1} * \Delta s_1 \qquad\qquad \Delta z = \frac{\delta z}{\delta s_2} * \Delta s_2 \tag{11}$$

$$\Delta z = \frac{\delta z}{\delta d_1} * \Delta d_1 \qquad\qquad \Delta z = \frac{\delta z}{\delta d_2} * \Delta d_2 \tag{12}$$

Equations 10, 11, 12 estimate the error in depth measurement due to uncertainty in rotation, zoom and pixel size respectively. MATLAB was used to compute these partial derivatives. Section 2.5 discusses the results.

2.5   Results of simulation

Table 3 lists the uncertainty in rotation, zoom and pixel size based on the accuracy of state of the art actuators and sensors. Table 4 shows the calculated errors in depth perception based on equations 10, 11, 12. These parameters were selected because they represent the limits of the state of the art actuators and sensors.

Off the shelf components	
Parameter	Value
Linear positioning, repeatability	5 microns
Angular positioning, repeatability	1.5 micro-radians
Pixel resolution	1 microns
Baseline	200 mm
Focal length of lens	20 mm

Table 3: Specifications of the components listed earlier in section 2.4

Error Estimation				
Distance from object to camera (meters)	Error due to rotation uncertainty per camera (microns)	Error due to focal length uncertainity per camera (microns)	Error due to discrete pixels per camera (microns)	Sum of all errors for both cameras (microns)
1	7.58	-0.093	0.06	15.09
2	30.08	-0.093	0.03	60.03
3	67.57	-0.093	0.02	135.01
4	120.08	-0.093	0.01	240.01
5	187.58	-0.093	0.01	374.99

Table 4: Error estimation based on off the shelf components. The first four columns give the error for one camera. The final column is double the sum of all errors to represent error from both cameras.

Table 4 shows that the largest source of error is rotational uncertainty. A small change in α_1 or α_2 has a huge impact on error. As described in equation 10, there is a linear relation between rotational uncertainty and error in depth estimation. If we could reduce the rotational uncertainty to 0.15 micro-radians then the error due to rotational uncertainty at 1 meter would drop to 0.758 microns. These results show that at a distance of five meters

with a rotational uncertainty of 1.5 micro radians, the error in depth measurement will be 375 microns. This is higher than the target of 100 microns. This estimate does not account for additional uncertainties such as backlash in joints, strain of materials, etc.

2.6 Positioning accuracy and sensor accuracy

For accurate depth estimation, it is important to know the exact rotation of the camera, the accuracy requirements of rotary sensing is high. The accuracy requirements of the rotary actuator are not as stringent as the accuracy requirements of the rotary encoder.

The objective of this section is to find out how accurately we need to rotate the camera to reliably cover a workspace (specifications described later) without missing any section. The calculations were performed for workspaces one - three meters wide placed five or ten metres away. The completely zoomed in field of view of each camera captures a five x five cm area of the workspace. Using triangulation, the aim is to calculate the rotation required to move the field of view to an adjacent five x five cm area. To make sure no position is missed, table 5 assumes a 50% overlap. For a five x five cm viewing area, table 5 calculates how much rotation is required to move the window by two and a half cm. At steep angles, more rotation is required to move the viewing area the same distance as compared to shallow angles. The width of the workspace was used to account for this. For a higher magnified view, a field of view of two x two cm area was also considered.

The results show that the most stringent position accuracy requirements with a two x two cm area is 367 micro radians which can be comfortably achieved with off the shelf actuators. Section 2.4 used rotary actuators with built in encoders. These have the advantage of providing a high accuracy closed loop positioning system. Rotary encoders offer similar performance but are more economical than rotary actuators with built in encoders.

Calculating required angular precision				
width of the workspace (m)	distance to the workspace (m)	field of view (cm)	Angular precision required in degrees	Angular precision required in micro radians
3	5	5	0.052	917.68
2	5	5	0.055	961.723
1	5	5	0.056	990.196
3	10	5	0.028	489.03
2	10	5	0.028	495.07
1	10	5	0.028	498.76
3	5	2	0.021	367.01
2	5	2	0.022	384.64
1	5	2	0.022	396.05

Table 5: Positioning precision requirements

2.7 Conclusion and Future scope

This work shows that active stereo vision is limited by rotational uncertainty. Sub 400 micron accuracy is possible at five meters assuming perfect mechanical linkages which do not contribute to error. Overcoming this limitation will allow high accuracy non contact measurement methods in the future.

This work considered the feasibility from a perspective of scientific capability. However for this setup to be a feasible replacement for measurement machines in industries, the cost of building a device must also be considered. Using prohibitively expensive, high performance rotary encoders and actuators would not make this a feasible replacement. The Renishaw REXM20 (Wotton-under-Edge, England) is a high performance encoder, each of these would cost $6000. To keep track of pan for both cameras, 2 encoders are needed. To tilt the setup to facilitate scanning in 3D, an additional encoder is needed.

Another factor to be considered for future calculations would be the optical limits of such a system. Assuming an ideal rotary encoder, the imperfections in lenses, abberations and diffraction limits would limit such a system.

Appendix

A   Anatomy of the eye

The anterior segment of the eye contains the cornea, iris, pupil, ciliary muscles, aqueous humour and the crystalline lens of the eye. Each of these will be defined starting from the outer regions of the eye, moving inwards. [12]

The outermost portion of the eyeball is called the **cornea** It is clear and responsible for $\frac{2}{3}$ of the refractive power of the eye. Since it needs to be transparent, the cornea does not have blood vessels. It gets nourishment from the tear ducts and the aqueous humour (defined later in this section)

The **iris** is a thin circular muscle which control the pupils. The **pupil** is the opening in the iris which can contract and dilate to control the amount of light entering the eye. This is analogous to varying the aperture of a camera.

Located behind the iris is the **ciliary body**. There are three types of muscles

1. Longitudinal/Meridonial

2. Oblique/Radial

3. Circular/sphincter

The **longitudinal** muscles control the opening and closing of the trabecular mesh-work. The trabecular mesh-work controls the drainage of a fluid called the aqueous humour. Build up of the aqueous humour can cause high intra-ocular pressure which can damage the retina. The **oblique** muscles widen the trabecular spaces. The **sphincter** muscles can contract to increase the convexity of the crystalline lens.

The **aqueous humor** is a clear fluid which nourishes the cornea. It also acts as a transport system for cellular metabolic excrement, inflammatory cells and drugs.

The **crystalline lens** is responsible for the remaining $\frac{1}{3}$ of the eyes refractive power. The convexity is controlled by the sphincter ciliary muscle. Adjusting the convexity allows the human eye to shift the focus between near and far objects.

The posterior segment of the eye consist of the vitreous humor, sclera, choroid, retina and the optic nerve.

The **vitreous humor** is a stagnant, colorless gel that fills the space between the crystalline lens and the retina. It does not refract light and does not affect the optical properties of the eye.

The **sclera** is the white opaque portion of the eye. The **choroid** is attached to the sclera by connective tissue. It supplies oxygen and nourishment to the retina. In addition, it regulates heat dissipation.

The **retina** is a circular disc located at the back of the eye. It has a diameter of 30 - 40 millimeters and a thickness of 0.5 millimeters. This is analogous to the CMOS or CCD sensor in a camera. There are three types of cell groups.

1. Photo receptors

2. Neuronal

3. Glial

The photoreceptors are further divided into rods and cone cells. The rod cells work in dim light and the cones work in bright light. The cone cells have three variations based on the

wavelength of light they respond to.

The **macula** is an oval shaped pigmented area on the retina, around five millimeters in width. It is responsible for our central vision and has a high density of photoreceptor cells. At the center of the macula, there is a small pit. This is called the **fovea** and is responsible for our sharp central vision.

The **optic nerve** allows the eye to communicate with the brain. It is attached to the retina at the optic disc. Since this spot on the retina does not have photo receptor cells, human vision has a blind spot at the optic disc. The optic disc is highly prominent on a fundus image. It is used as a reference point while trying to orient fundus cameras.

B   Parts and selection criteria

This section discusses the specifications of the parts used and reasons for selecting them. Apart from the regular beam splitter, all parts were used in the setup that was built as shown in figure 5. The regular beam splitter specifications were used for simulations.

Parts used			
Part	**Vendor**	**Part number**	**Link**
Lenses	Edmund Optics	#89-200	Link
Polarizing beam splitter	Edmund Optics	#48-545	Link
Camera	Edmund Optics	#15-837	Link
Variable focal length lens	Edmund Optics	#86-573	Link
Training Eye	Gulden Ophthalmics	#15173	Link
Waveplate / Retarder	Edmund Optics	#14-723	Link

B.1   Lenses

The objective lens of the fundus camera is also the objective lens of the virtual reality headset. The 50mm Dia. x 50mm FL VIS-EXT Coated, Double-Convex Lens offered by Edmund optics was used. There are a few factors to consider while selecting this lens.

1. Virtual reality headsets work by creating a magnified virtual image of a screen at a comfortable viewing distance. The distance between the screen and the lens must be a little less than one focal length.

2. The f-ratio is defined as the $\frac{focal\ length\ of\ the\ lens}{diameter\ of\ the\ lens}$ [26]. This parameter describes the light gathering power of a lens. A shorter f-ratio indicates a better light gathering ability.

3. A shorter focal length will result in a wider field of view while imaging the eye. This is desirable because a larger portion of the retina can be imaged.

4. If the lens diameter is too small, the immersive experience of the Virtual reality headset is lost [27].

The size of the VR headset also determines the field of view of the resulting image. A large VR headset can accommodate a large beamsplitter which allows imaging the retina at sharper angles, increasing the field of view. However if the VR headset is too large, it will become unwieldy for the patient. Keeping this in mind, we used a biconvex lens (Edmund optics, Part: 89-200, New Jersey) with a focal length of 50mm and a diameter of 50mm as our objective lens.

Anti reflection coatings are designed so that back reflections destructively interefere with each other. Edmund optics offers a variety of coating options, VIS-EXT was selected because it performs well throughout the visible spectrum compared to the others as per the manufacturer.

B.2   Camera

The camera and lens choices were made after great deliberation. This project used a FLIR Blackfly USB3 Camera (BFS-U3-17S7C-C).

There were a few factors to consider while selecting a camera as listed below. The main objectives were good low light performance and high frame rates.

1) Color Cameras

After light passes through the camera lenses, it falls on a photosensitive sensor. The intensity of light that falls on the surface is directly proportional to the photoelectric current generated. In a color camera, filters are used to segregate the 3 primary colors - red, green and blue.

Gray scale is better for low light applications because light is not lost in the filtration process. However color fundus imaging has a diagnostic purpose. Some diseases require color images to be diagnosed [28].

2) Sensor size and resolution

A higher resolution sensor will produce clearer images because the disparity between pixel locations is less. To create high resolution sensors, small pixels are used. A larger pixel will interact with more light giving it better low light performance. Prioritizing low light performance we chose a large pixel size with an area of 45 square micro-meters (Sony IMX425) as opposed to the 12 square micro-meters pixels that they offer. The resolution of this sensor is 1.7 megapixels. The sensor is sized diagonally at 1.1 inches.

3) Quantum efficiency, temporal noise and saturation capacity

To generate a digital image, the first step is to convert photons to electrons. The efficiency of this conversion is called the quantum efficiency [29]. Good low light performance requires a high quantum efficiency. The Sony IMX425 is a 3rd generation Sony Pregius sensor. Compared to the other generations, it shows higher quantum efficiency for most of the visible spectrum. It is important to note that a newer sensor generation does not indicate an overall improvement. The 4th generation sensor offers higher resolutions compared to the 3rd generation. However, the 3rd generation has better low light performance.

Each pixel has a well which stores the electrons generated. These wells have limits defined by the saturation capacity [30]. Once this limit has been reached, no more electrons will be stored.This was not an important parameter for us since we expected our imaging to be at very low levels of light.

Once the electrons are stored in the well, they are measured to assign a signal value to the

pixel. The error in this measurement is called noise [31]. This is an important parameter for low light imaging. Signals in a low noise sensor can be amplified further before becoming unreliable.

4) Exposure time and frame rate

The exposure time determines how long a camera shutter stays open to allow light to fall on the sensor. This is inversely proportional to the frame rate. Lower exposure times allow more frames to be captured per second.

Microsaccades are tiny involuntary eye movements. Taking images with an exposure time of less than 0.67 seconds minimizes the chances of movement between frames [10]. A high frame rate corresponds to a low exposure time which is desirable.

On the other hand, high exposure times allow more light to be captured. This is desirable for good low light imaging. A balance needs to be struck here. Although the camera used is rated for 196 frames per second, we found that a frame rate of 20-50 frames per second was required for reliable imaging.

5) Global shutter and Rolling shutters

A camera with a global shutter exposes all pixels of the sensor to light simultaneously. A rolling shutter exposes the sensor one line of pixels at a time.

A global shutter makes it easier to image fast moving objects. A microsaccade during a rolling shutter sensor exposure will corrupt the image. We chose to use a camera with a global shutter.

B.3 Camera Lens and Aperture

Machine vision cameras have mounts onto which lenses can be attached. We chose the 35mm Focal Length, HP Series Fixed Focal Length Lens made by Edmund Optics.

The 35mm focal length was selected based on our initial designs to work with the objective and relay lenses selected. The lens has a variable aperture which can be manually adjusted.

The aperture of the camera defines the size of the hole that allows light to enter the camera. A wider aperture allows more light into the camera, this is desirable for low light imaging. However a smaller aperture gives a larger depth of field. The depth of field determines how much distance in front and behind the focal plane is in focus. A small aperture would require less adjustment of the camera's focal plane. A balance needs to be struck here between the need for light and ease of focus. The lens aperture can be adjusted from f/1.8 to f/16. f/16 is the smallest aperture size this lens offers. Our experiments showed that f/8 provided decent images.

B.4 Artificial eye

The timberlake training (Gulden Ophthalmics, Part:15173, Philadelphia, USA) was used to test our setup. It has 2 concentric cylinders which slide into each other. The larger cylinder holds the lens which simulates the cornea.The smaller cylinder holds a plate which has an image of the retina.

B.5 Waveplate/Retarder

A retarder changes the polarization state of light passing through it. These are generally birefrigent materials whose refractive indices are dependent on the orientation. When light

passes through it, the phase difference between perpendicular components change because they are travelling at different speeds. This changes the polarization.

Edmund optics offers $\dfrac{\lambda}{2}, \dfrac{\lambda}{4}, 1\lambda$ retarder films. Each of them shift the phase by different amounts. The quarter wavelength film was selected because our design called for conversion from circularly polarized to linearly polarized.

B.6 Beam splitter

The two designs vary in this aspect. The setup as shown in figure 5 uses a polarizing beam splitter. The simulation assumes a regular beam splitter.They are generally offered as cubes or plates. Cubes are offered in larger sizes which help with the field of view, however plates were selected to keep the weight of the headset down.

Polarizing beam splitter

The largest off the shelf polarizing plate beam splitter available measures 25mm x 25mm. It transmits 85 - 90 % of p-polarized light and reflects 85 - 90% of s-polarized light.

Regular beam splitter

A 50mm x 50mm plate beam splitter was selected for the second design. Larger beam splitters are available but these dimensions are limited by the size of the headset. After building our first setup, we realized that reflections from the retina are diffusive. The polarization of light is not maintained as in specular reflections. A polarizing beam splitter is not required.

References

[1] R. JMJ, "Leading causes of blindness worldwide," *Bull Soc Belge Ophtalmol*, vol. 283, pp. 19–25, 2002.

[2] S. S. Kanse and D. M. Yadav, "Retinal fundus image for glaucoma detection: A review and study," *Journal of Intelligent Systems*, vol. 28, no. 1, pp. 43–56, 2019.

[3] J. P. Diamond, M. McKinnon, C. Barry, D. Geary, I. L. McAllister, P. House, and I. J. Constable, "Non-mydriatic fundus photography: a viable alternative to fundoscopy for identification of diabetic retinopathy in an aboriginal population in rural western australia?" *Australian and New Zealand journal of ophthalmology*, vol. 26, no. 2, pp. 109–115, 1998.

[4] M. SIT and A. V. LEVIN, "Direct ophthalmoscopy in pediatric emergency care," *Pediatric emergency care*, vol. 17, no. 3, pp. 199–204, 2001.

[5] G. Jardine. How to use the direct ophthalmoscope. [Online]. Available: https://morancore.utah.edu/basic-ophthalmology-review/how-to-use-the-direct-ophthalmoscope/

[6] H.-J. Kong, J. Seo, M. Jeong, Hwang, and H. C. Kim, "Indirect ophthalmoscopic stereo video system using three- dimensional lcd," 02 2009.

[7] E. DeHoog and J. Schwiegerling, "Fundus camera systems: a comparative analysis," *Applied optics*, vol. 48, no. 2, pp. 221–228, 2009.

[8] J. Schmitt, "Optical coherence tomography (oct): a review," *IEEE Journal of Selected Topics in Quantum Electronics*, vol. 5, no. 4, pp. 1205–1215, 1999.

[9] A. F. Fercher, W. Drexler, C. K. Hitzenberger, and T. Lasser, "Optical coherence tomography-principles and applications," *Reports on progress in physics*, vol. 66, no. 2, p. 239, 2003.

[10] E. DeHoog and J. Schwiegerling, "Optimal parameters for retinal illumination and imaging in fundus cameras," *Applied optics*, vol. 47, no. 36, pp. 6769–6777, 2008.

[11] P. C. Ng and J. J. Oliver, "Anatomy of the eye," in *Handbook of Emergency Ophthalmology*. Springer, 2018, pp. 1–12.

[12] E. Addo, O. A. Bamiro, and R. Siwale, "Anatomy of the eye and common diseases affecting the eye," in *Ocular drug delivery: Advances, challenges and applications*. Springer, 2016, pp. 11–25.

[13] M. D. Abramoff and M. Niemeijer, "The automatic detection of the optic disc location in retinal images using optic disc location regression," in *2006 International Conference of the IEEE Engineering in Medicine and Biology Society*. IEEE, 2006, pp. 4432–4435.

[14] M. S. d. Almeida and L. A. Carvalho, "Different schematic eyes and their accuracy to the in vivo eye: a quantitative comparison study," *Brazilian Journal of Physics*, vol. 37, no. 2A, pp. 378–387, 2007.

[15] D. A. Atchison and L. N. Thibos, "Optical models of the human eye," *Clinical and Experimental Optometry*, vol. 99, no. 2, pp. 99–106, 2016.

[16] E. Villegas, L. Carretero, and A. Fimia, "Le grand eye for the study of ocular chromatic aberration," *Ophthalmic and Physiological Optics*, vol. 16, no. 6, pp. 528–531, 1996.

[17] S. Richtberg and R. Girwidz, "Use of linear and circular polarization: The secret lcd screen and 3d cinema," *The Physics Teacher*, vol. 55, no. 7, pp. 406–408, 2017.

[18] D. Bublitz, M. J. Everett, C. Farkas, M. Kempe, Y. Qiu, and T. Schmitt-Manderbach, "Systems and methods for broad line fundus imaging," Oct. 4 2016, uS Patent 9,456,746.

[19] R. A. Orozco, "Pyoptools." [Online]. Available: https://github.com/cihologramas/pyoptools

[20] M. Babic, M. A. Farahani, and T. Wuest, "Image based quality inspection in smart manufacturing systems: A literature review," *Procedia CIRP*, vol. 103, pp. 262–267, 2021.

[21] G. F. Poggio and T. Poggio, "The analysis of stereopsis," *Annual review of neuroscience*, vol. 7, no. 1, pp. 379–412, 1984.

[22] S. B. Kang, J. Webb, and C. Zitnick, "An active multibaseline stereo system with real-time image acquisition," 11 1999.

[23] D. Wan and J. Zhou, "Stereo vision using two ptz cameras," *Computer Vision and Image Understanding*, vol. 112, no. 2, pp. 184–194, 2008.

[24] W. Jang, C. Je, Y. Seo, and S. W. Lee, "Structured-light stereo: Comparative analysis and integration of structured-light and active stereo for measuring dynamic shape," *Optics and Lasers in Engineering*, vol. 51, no. 11, pp. 1255–1264, 2013.

[25] A. Miks and J. Novak, "Analysis of two-element zoom systems based on variable power lenses," *Opt. Express*, vol. 18, no. 7, pp. 6797–6810, Mar 2010. [Online]. Available: http://opg.optica.org/oe/abstract.cfm?URI=oe-18-7-6797

[26] D. Lynden-Bell, "Exact optics: a unification of optical telescope design," *Monthly Notices of the Royal Astronomical Society*, vol. 334, no. 4, pp. 787–796, 2002.

[27] G. Robertson, M. Czerwinski, and M. Van Dantzich, "Immersion in desktop virtual reality," in *Proceedings of the 10th annual ACM symposium on User interface software and technology*, 1997, pp. 11–19.

[28] M. K. Nath and S. Dandapat, "Techniques of glaucoma detection from color fundus images: A review," *International Journal of Image, Graphics and Signal Processing*, vol. 4, no. 9, p. 44, 2012.

[29] F. Sigernes, M. Dyrland, N. Peters, D. A. Lorentzen, T. Svenøe, K. Heia, S. Chernouss, C. S. Deehr, and M. Kosch, "The absolute sensitivity of digital colour cameras," *Optics express*, vol. 17, no. 22, pp. 20 211–20 220, 2009.

[30] T. Narabu, "Advances in the image sensor: The critical element in the performance of cameras," in *AIP Conference Proceedings*, vol. 1321, no. 1.   American Institute of Physics, 2011, pp. 113–118.

[31] P. A. Cheremkhin, N. N. Evtikhiev, V. V. Krasnov, V. G. Rodin, and S. N. Starikov, "Modified temporal noise measurement method with automatic segmentation of nonuniform target, its accuracy estimation, and application to cameras of different types," *Optical Engineering*, vol. 53, no. 10, p. 102107, 2014.